

Rhodium-based metal-organic polyhedra assemblies for selective CO₂ photoreduction.

Ashta C. Ghosh,^{†,Δ} Alexandre Legrand,^{#,Δ} Rémy Rajapaksha,[†] Gavin A. Craig,^{#,♦} Capucine Sassoie,[↓] Gábor Balázs,[‡] David Farrusseng,[†] Shuhei Furukawa,^{#,*} Jérôme Canivet,^{†,*} Florian M. Wisser^{‡,*}

[†] Université de Lyon, Université Claude Bernard Lyon 1, CNRS, IRCELYON - UMR 5256, 2 Avenue Albert Einstein, 69626 Villeurbanne Cedex, France.

[#] Institute for Integrated Cell-Material Sciences (WPI-iCeMS), Kyoto University, Yoshida, Sakyo-ku, Kyoto 606-8501, Japan.

[↓] Sorbonne Université, Chimie de la Matière Condensée de Paris - UMR 7574, 4 Place Jussieu, 75005 Paris, France

[‡] Institute of Inorganic Chemistry, University of Regensburg, 93040 Regensburg, Germany.

KEYWORDS. CO₂ reduction, dirhodium paddlewheels, formic acid, heterogeneous photocatalysis, metal-organic polyhedra

ABSTRACT: Heterogenization of molecular catalysts via their immobilization within extended structures often results in a lowering of their catalytic properties due to a change in their coordination sphere. Metal-organic polyhedra (MOPs) are an emerging class of well-defined hybrid compounds with a high number of accessible metal sites organised around an inner cavity, making them appealing candidates for catalytic applications. Here we demonstrate a design strategy that enhances the catalytic properties of dirhodium paddlewheels heterogenized within a MOP (Rh-MOP) and its three-dimensional assembled supramolecular structures, which proved to be very efficient catalysts for the selective photochemical reduction of carbon dioxide to formic acid. Surprisingly, the catalytic activity per Rh atom is higher in the supramolecular structures than in its molecular sub-unit Rh-MOP or in Rh-MOF, and yields turnover frequencies of up to 60 h⁻¹ and production rates of approx. 76 mmole formic acid per gram of catalyst per hour, unprecedented in heterogeneous photocatalysis. The enhanced catalytic activity is investigated by X-ray photoelectron spectroscopy and electrochemical characterization, showing that self-assembly into supramolecular polymers increases the electron density on the active site, making the overall reaction thermodynamically more favourable. The catalyst can be recycled without loss of activity and with no change of its molecular structure as shown by pair distribution function analysis. These results demonstrate the high potential of MOPs as catalysts for the photoreduction of CO₂ and open a new perspective for the electronic design of discrete molecular architectures with accessible metal sites for the production of solar fuels.

INTRODUCTION

A fruitful strategy in the design of molecularly-defined heterogeneous catalysts is the immobilization of isolated active sites within a host framework whose intrinsic porosity ensures the accessibility of the active site. Importantly and beyond technical advantages like direct catalyst separation from product, heterogenization can also stabilize accessible metal sites that act as single atom catalysts, avoiding the formation of metal clusters and maintaining a high concentration of active sites.^{1–6}

Thus, the controlled structuration of accessible metal sites as a key catalytic component in a porous framework confers appealing catalytic properties combining high site density and stabilization with active site accessibility on the corresponding materials. However, the integration of catalytically active centres into a solid support often results in an intrinsic reduction of their activity compared to their homogeneous molecular counterparts.^{3,7,8} The reasons for this decrease in catalytic activity are not yet fully understood. Recently we demonstrated that one crucial factor resulting in a lower catalytic activity after heterogenization is the change in the electron density on the catalytically active site caused by the heterogenization itself.⁹

In the context of catalytically active accessible metal sites, Rh₂^{II,II} paddlewheel complexes, in which the removal of labile

ligands from the axial position of the paddlewheel can give access to open Rh metal sites, stand out by their high chemical stability as well as their variety of accessible redox states, including Rh₂^{II,I} and Rh₂^{II,III} oxidation states.^{10,11} Consequently, Rh₂^{II,II} paddlewheel complexes have attracted interest in a large range of catalytic reactions,¹¹ including cyclopropanation,^{12,13} hydrogenation,^{14–17} ethylene dimerization,¹⁸ or photocatalytic hydrogen evolution reaction.^{10,11,19,20} So far, the heterogenization of the Rh₂^{II,II} paddlewheel as a catalytic centre has been limited to their immobilization within supramolecular structures (through non-covalent interaction) or coordination polymers and metal-organic frameworks (MOFs). A controlled arrangement of Rh₂^{II,II} paddlewheels has recently been reported in metal-organic cages, also called metal-organic polyhedra (MOPs), which are discrete molecular structures, self-assembled from bent ligands and metal precursors.^{21–23} As one of the smallest porous units, MOPs have been used as templates to accommodate and control properties of various guests, and have shown promising applications in, sorption, separation, and sensing.^{21,24–27} In catalytic applications MOPs have been used mostly as nanocontainers, encapsulating catalytically active species,²⁸ or as nanoreactors, with grafted organocatalysts or inorganic complexes to their linker backbone.^{29–32} So far, the use of the secondary building unit of metal-organic polyhedra as a

catalytic centre is still scarce,^{33–35} and their potential as a **catalyst in a photocatalytic system, a system that contains a catalyst and a photosensitizer,**³⁶ is as yet unexplored.

Here, we explore the catalytic activity of the pre-formed MOP [Rh₂(bdc)₂]₁₂ (bdc = benzene-1,3-dicarboxylate) and their assembled supramolecular structures formed by coordination with bix (bix = 1,4-bis(imidazol-1-ylmethyl)benzene) as ditopic N-donor linkers. Depending on the amount of N-donor linker, the materials are obtained as colloidal particles (Rh-CPP) or aerogels (Rh-SAG, Figure 1).³⁷ As heterogeneous catalysts in

the photocatalytic reduction of CO₂ to formic acid, they yield unexpectedly high catalytic activities, outperforming both molecular Rh₂^{II,II} paddlewheel complexes and other heterogeneous photocatalysts. We use pair distribution function analysis, XPS, *in situ* EPR spectroscopy and electrochemical measurements to rationalize these findings. The key favourable properties of these catalysts are their high density of Rh active sites, their high accessibility due to the cage structure of the MOP, and the increased electron density of the active sites induced by their immobilization in a supramolecular polymer with a suitable electron donating linker.

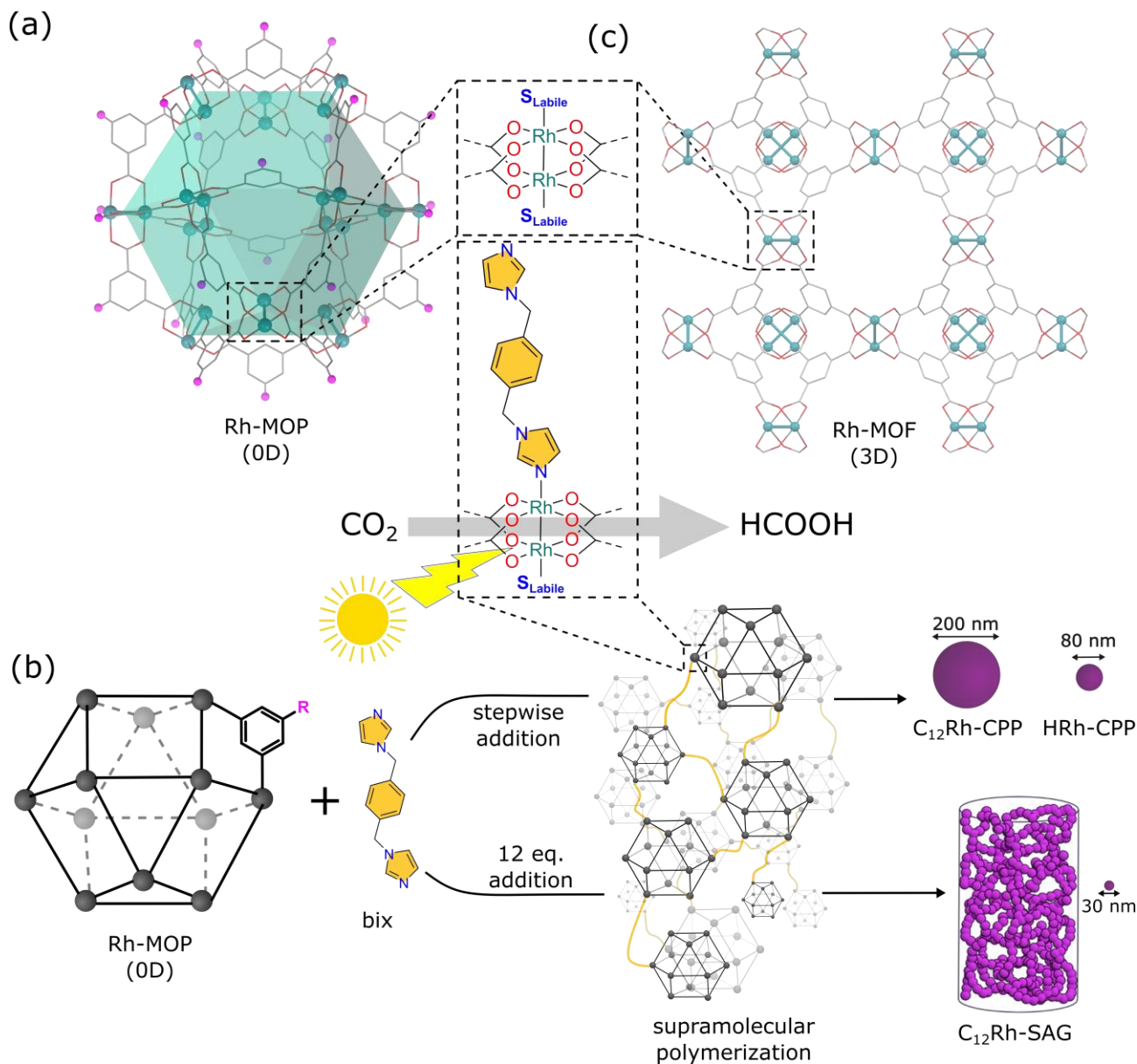


Figure 1. Schematic representation of (a) the Rh-MOP, [Rh₂(R-bdc)₂]₁₂ (R = 5-dodecoxy (C₁₂) or H), with the green polygon highlighting the cuboctahedral geometry of the cage and the purple atoms the substituent groups in the five positions of the isophthalic acid (R-bdc). The structure is calculated from the single crystal data of [Rh₂(H-bdc)₂]₁₂.³⁸ (b) Schematic representation of the supramolecular polymerization reaction between Rh-MOP and bix, which leads to the formation of colloidal particles (Rh-CPP) when bix is added stepwise or to the formation of a colloidal gel network when 12 eq. of bix are added. The gel is then transformed into the corresponding colloidal aerogel (Rh-SAG) after solvent exchange and ScCO₂ drying process. (c) Schematic representation of the Rh-MOF, [Rh₃BTC₂]_n, derived from isostructural Cu₃BTC₂ (because of the absence of experimental [Rh₃BTC₂]_n structure) view along the crystallographic a axis (CCDC 827934). H-atoms are omitted for clarity. Color code: Rh green, O red and C grey. The Rh-MOP and Rh-MOF possess two axial, accessible metal sites in the rhodium paddlewheel, while for the assembled colloidal particles and aerogel based on Rh-MOP building blocks, the metal nodes are partially coordinated by bix molecules in the exohedral axial site (at the MOP surface).

RESULTS AND DISCUSSION

Design of Rh₂^{III} paddlewheel catalysts. Previously, we reported the self-assembly of isophthalic acid derivatives with rhodium paddlewheel precursors (Rh₂(OAc)₄) to form stable rhodium-based cuboctahedral MOPs, which possess an internal cavity with a diameter of ~ 1.2 nm and window openings of 0.4 and 0.7 nm for trigonal and square shaped apertures respectively, as determined using pywindow software, which allows for structural characterization of porous materials.³⁹ In case of isophthalic acid (H-bdc) as ligand the MOP [Rh₂(H-bdc)₂]₁₂ is obtained,³⁸ and in case of 5-dodecoxybenzene-1,3-dicarboxylic acid (C₁₂-bdc) the MOP [Rh₂(C₁₂-bdc)₂]₁₂,⁴⁰ called hereafter **HRh-MOP** and **C₁₂Rh-MOP**, respectively (Figure 1a). In the case of **HRh-MOP**, it is necessary to solubilize the cage through the coordination of 1-dodecyl-1H-imidazole (diz), to the exohedral axial metal sites of the MOP, prior to any supramolecular polymerization reaction. Further reaction of the exohedral Rh(II) ions of the Rh-MOPs with bix as a ditopic N-donor ligand drives their self-assembly into supramolecular polymers (Figure 1b).³⁷ During the stepwise addition of bix (see SI section S2 for details), the supramolecular polymers can be obtained as spherical coordination polymer particles (CPP) with an average diameter of 206 ± 63 nm and 79 ± 18 nm for **C₁₂Rh-CPP** and **HRh-CPP**, respectively (Figure S6a, b). When adding the Rh-MOP to 12 molar equivalents of bix, a colloidal gel network, made of particles of 30 nm, is formed. Further processing of the gel with supercritical CO₂ dryer lead to the formation of a supramolecular aerogel after solvent removal (**C₁₂Rh-SAG**, Figure S9).³⁷ The **C₁₂Rh-CPP** has an average composition of [Rh₂(C₁₂-bdc)₂]₁₂(bix)_{5.1} (Figure S7a), while the content of bix linker is approximately double in the aerogel, giving a composition of [Rh₂(C₁₂-bdc)₂]₁₂(bix)_{9.8} (Figure S10).³⁷ For **HRh-CPP**, the composition is [Rh₂(H-bdc)₂]₁₂(bix)_{7.9}(diz)_{2.7} (Figure S7b). All supramolecular polymers are built from well-defined building-blocks but lack long range order.

In the Rh-CPP and Rh-SAG materials, the endohedral axial rhodium atom of each Rh paddlewheel is an accessible metal site pointing towards the inside of the porous cage, while the exohedral one can be coordinated by imidazole moiety from either bix or diz. For comparison, we also synthesized a Rh-paddlewheel-containing Rh-MOF, [Rh₃(BTC)₂]_n,⁴¹ which was obtained by reacting Rh₂(OAc)₄ with benzene-1,3,5-tricarboxylic acid (H₃BTC) in aqueous acetic acid at 150 °C. In this material, the Rh₂ paddlewheels are linked in all three dimensions by bridging BTC³⁻ molecules, resulting in a rigid, crystalline, porous framework (Figure 1c), similar to the copper analogue [Cu₃(BTC)₂]_n,⁴² and properties in line with results from literature (SI section S2, Figure S15 for further characterization).⁴¹ In a similar fashion to the Rh-MOPs, the Rh-MOF should arrange Rh paddlewheels with accessible metal sites in the axial positions into cuboctahedral geometry; however, it is difficult to accurately estimate the pore size due to the lack of the crystal structure of Rh-MOF ($d_{\text{pore}} \approx 1.1$ nm, estimated using pywindow software³⁹). With the exception of **C₁₂Rh-MOP**, all of the materials are porous towards nitrogen at 77 K, with apparent surface areas of 20 m²/g, 100 m²/g, 160 m²/g and 880 m²/g for **C₁₂Rh-CPP**, **HRh-CPP**, **C₁₂Rh-SAG** and **HRh-MOP**, respectively (Figure S11), and 870 m²/g for Rh-MOF (Figure S15a). **The sharp decrease of the surface area toward N₂ for HRh-CPP compared to HRh-MOP is due to presence of alkyl-chain from the remaining diz decorating the surface of the cage, which reduce the sorption properties of the material by partially blocking its pore.** The pore size distribution (PSD) demonstrates that

all of the samples have pores in the microporous/mesoporous range. In particular, **HRh-MOP** and **HRh-CPP** have a microporosity, in good agreement with the dimensions of the cuboctahedral cage (Figure S12).⁴³ In addition, the supramolecular systems present extrinsic porosity arising from the free volume between the MOPs within the colloidal particles. The smaller surface areas observed for the C₁₂Rh-systems compared to HRh-systems as well as Rh-MOF are explained by the bulky alkyl chain hindering the gas diffusion to the MOP cavity and occupying free volume in the materials. It is worth noting that Rh-MOF, Rh-MOPs and the supramolecular polymers **C₁₂Rh-CPP**, **C₁₂Rh-SAG** and **HRh-CPP** are accessible for CO₂.^{37,41,44} For the C₁₂Rh-MOP series, CO₂ uptake at 195 K increases from 20 mol(CO₂)/mol(C₁₂Rh-MOP) in **C₁₂Rh-MOP** to more than 32 mol(CO₂)/mol(C₁₂Rh-MOP) in **C₁₂Rh-CPP** and **C₁₂Rh-SAG**. The increase in CO₂ capacity is caused by the additional extrinsic porosity in the supramolecular materials.³⁷ More important for application in liquid catalysis is the materials interaction with the solvent used. All materials are porous towards acetonitrile at 298 K (Table S1), the highest pore volume achieved for RhMOF with 0.58 cm³/g (Figure S15b). **HRh-MOP** and **HRh-CPP** possess slightly lower pore volumes of approx. 0.43 and 0.53 cm³/g, respectively (Figure S13). Due to the larger molar mass of the cuboctahedral building block, **C₁₂Rh-MOP**, **C₁₂Rh-CPP** and **C₁₂Rh-SAG** possess lower pore volumes of 0.29, 0.25 and 0.22 cm³/g, respectively (Figure S13).

Photocatalytic CO₂ reduction. In the context of greenhouse gases reduction and solar fuel production, Rh paddlewheel-based materials have never been reported as CO₂ reduction catalysts so far, **Mizuno and co-workers reported the use of dissolved Rh₂OAc₄ as molecular catalyst for the silylation of CO₂.**⁴⁵ Thus, we evaluated the performance of the **Rh-MOPs**, as well as that of solid **Rh-CPPs** and **Rh-SAG**, as catalysts in the photochemical CO₂ reduction in the presence of Ru(bpy)₃Cl₂ as photosensitizer and triethanolamine (TEOA) as sacrificial electron donor. For the sake of comparison, the catalytic behaviour of Rh-paddlewheels has also been studied in molecular Rh₂(OAc)₄ and Rh-MOF.

The photocatalytic CO₂ reduction experiments were carried out in a mixture of acetonitrile as solvent and TEOA as proton and electron donor under a solar simulator as light source. **All materials showed catalytic activity for the transformation of CO₂ into formic acid as the only carbon containing product (Figure 2a), as no traces of CO, CH₃OH or CH₄ were detected (vide infra, for more details see SI section 6.3).** To calculate the catalytic activity, we considered that – consistent with reports from hydrogen evolution reaction^{10,11,20} and electrochemical CO₂ reduction¹¹ – the catalytically active site consists of one Rh₂ paddlewheel unit, independently of whether there are one or two accessible metal sites per paddlewheel. The lowest catalytic activity was obtained with the Rh-MOF, with a turnover frequency (*TOF*) of only 5 h⁻¹ and a production rate *R* of up to 10.1 mmol_{formic acid}/g_{cat}/h (Figure 2a, Table S6, & Table S7). In a clear contrast, the supramolecular polymers, Rh-CPPs and Rh-SAG, achieved *TOFs* of up to 59 h⁻¹ (Figure 2a, *R* = 76 mmol_{formic acid}/g_{cat}/h, Table S6), independently of their apparent surface area. Gas phase analysis of the reaction head space as well as ¹³C NMR spectra from carbon-13 labelling experiments using ¹³CO₂ (99 atom-% ¹³C), confirmed that formic acid is the only carbon containing reduction product. **No traces of ¹³CH₃OH at approx. 50 ppm⁴⁶ nor of dissolved ¹³CO⁴⁷ at 185 ppm or ¹³CH₄ at -4.6 ppm⁴⁶ were detected (Figure S32), in**

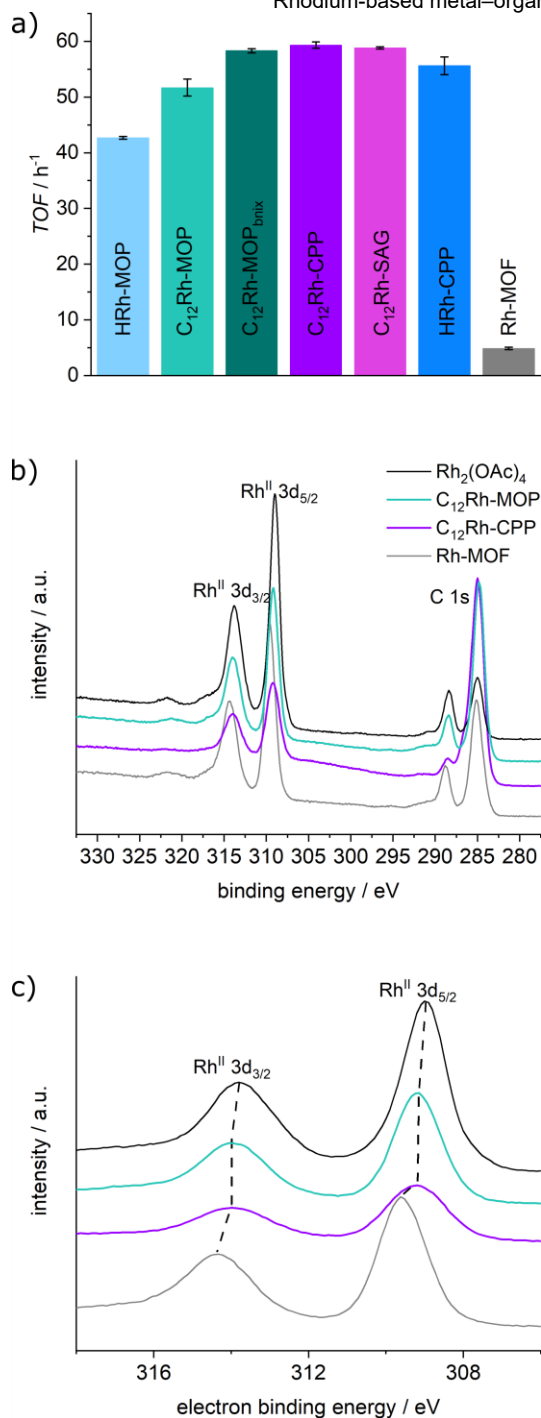


Figure 2. a) Overview of catalytic activity in photocatalytic CO₂ reduction over various Rh₂-based catalysts in the presence of Ru(bpy)₃Cl₂ as photosensitizer. Reaction conditions: 0.05 mM catalyst, 1 mM Ru(bpy)₃Cl₂ in ACN : TEOA (5 : 1, V : V), 2 h, ABA class solar simulator without filter. b) XPS spectra of Rh₂BTC₂, Rh₂(OAc)₄, C₁₂Rh-MOP and C₁₂Rh-CPP showing C 1s and Rh 3d binding energy region and c) enlarged region of Rh 3d binding energy. Change in the electron binding energy is highlighted by the dotted line. Deconvoluted spectra are provided in Figure S15.

line with IR spectra of the gas phase after catalysis, showing no traces of CO or CH₄ (Figure S33). From the corresponding ¹H NMR spectra, the nature of the carbon atom to which the C-H formic acid proton (HCOOH) is bound, and thus the carbon

source for formic acid formation, can be unambiguously distinguished by the ¹H-¹³C *J*-coupling through the C-H bond. In the ¹H NMR spectrum of the carbon-13 labeling experiment, the HCOOH is detected as a doublet with a ¹J_{C-H} coupling constant of 189 Hz. The H¹²COOH singlet is detected only in traces (1%), stemming from the 1 atom-% ¹²CO₂ impurity in the ¹³CO₂. Thus, formic acid was produced exclusively from CO₂, implying that the network had not decomposed (for further details see SI, section 6.3, Figure S32).

Rationalization of catalytic activities. Despite their different morphology and porosity, C₁₂Rh-CPP and C₁₂Rh-SAG show the same catalytic activity (*TOF* = 59 h⁻¹), slightly higher than their molecular building block C₁₂Rh-MOP (*TOF* = 52 h⁻¹). The main structural difference between the isolated C₁₂Rh-MOP and the 3D materials C₁₂Rh-CPP and C₁₂Rh-SAG results from the coordination of the bix ligands to the exohedral axial positions of the C₁₂Rh-MOP thus (i) introducing extrinsic porosity to the materials and (ii) changing the molecular environment of the active site (Figure 1). In order to mimic the coordination by bix N-atoms in C₁₂Rh-CPP and C₁₂Rh-SAG solids, the exohedral Rh atoms of the pristine C₁₂Rh-MOP were capped by reaction with 12 equivalents of monodentate 1-benzylimidazole (bnix) to yield [Rh₂(C₁₂-bdc)₂]₁₂(bnix)₁₂ (C₁₂Rh-MOP_{bnix}) as a molecular model of the corresponding CPP and SAG (Figure S2). C₁₂Rh-MOP_{bnix} gave rise to an increased catalytic activity (*TOF* = 58 h⁻¹), very similar to the activity observed for C₁₂Rh-CPP and C₁₂Rh-SAG. We thus infer from this trend that (i) the reaction is not limited to surface processes in the heterogeneous supramolecular polymers and (ii) the inner part of the heterogeneous catalysts is indeed accessible for the reactants, including TEOA.

Importantly, the coordination of monotopic bnix molecules to the exohedral Rh atoms of the Rh₂ paddlewheel slightly increases the electron density on Rh centres, resulting in higher catalytic activity (*vide infra*). It is worth noticing that the substituents of the bdc linker in the 5-position of the Rh-MOP have an effect on the catalytic activity. Indeed, when the alkoxy group of the C₁₂Rh-MOP is replaced by hydrogen (HRh-MOP), the *TOF* and production rate show a slight decrease (*TOF* = 43 h⁻¹ vs. 52 h⁻¹ for C₁₂Rh-MOP). As for C₁₂Rh-MOP, heterogenization of HRh-MOP in the corresponding HRh-CPP material results in an increase of *TOF* to approx. 56 h⁻¹ (Table S6, entry 31). The slightly higher catalytic activities of the C₁₂Rh-MOP based materials can be explained by an higher electron density on the active Rh site in those materials, caused by the higher electron donating properties of the alkyl chain when compared to the hydrogen atom in the 5-position of the isophthalate linkers.^{9,48}

Despite having structurally similar Rh-paddlewheel building units, the Rh-MOP molecular systems show a two-fold increase in *TOF* compared to the Rh₂(OAc)₄ (Table S6, entries 4, 40 & Table S7, entries 1, 9). Here we note that during photocatalysis Rh₂(OAc)₄ decomposes into Rh nanoparticles, as evidenced by TEM analysis of the reaction mixture (see Figure S29). On the other hand, we did not observe any indication of decomposition in the Rh-MOP molecular systems, e.g. leaching of paramagnetic Rh species or formation of Rh nanoparticles. Thus, the increase in turnover numbers is most likely caused by a stabilisation of the dirhodium moiety within the Rh-MOPs. Similarly, for the extended structures, the Rh-MOP-based catalysts show a twelve-fold increase in *TOF* compared to the Rh-MOF. To

understand these differences in catalytic activity, X-ray photoelectron spectroscopy (XPS) is an asset to investigate changes in electron density on the active site. Indeed, the catalytic activity in heterogeneous molecular photocatalysis in a series of structurally comparable heterogenized catalysts has recently been demonstrated to depend on the electron density of the active site. We recently reported that for Rh catalysed CO₂ reduction reaction, a decrease in rhodium electron binding energy (*EBE*), corresponding to a higher electron density on the rhodium, results in a higher catalytic activity.⁹ Here we observed similar behaviour. Rh atoms in the Rh-MOF show a significant higher electron binding energy (309.6 eV) compared to the Rh atoms in the Rh-MOP (309.3 eV) or the Rh-CPP and Rh-SAG (309.2 eV, Figure 2b, c & Figure S16). Thus, the lower catalytic activity of the Rh-MOF can be attributed to the lower electron density on the active site (higher *EBE*), directly affecting the reaction rate. This difference in *EBE* is directly related to replacing the electron donating substituents in the 5 position of the benzene moiety in Rh-MOPs by an electron withdrawing Rh-carboxylate. This is further reflected by an increase in the substituents' Hammett constant, an empirical descriptor of the electron density, for the more electron withdrawing group.^{5,9,48,49}

The Rh-MOP based polymers outperform the most active heterogeneous photocatalytic systems for the selective transformation of carbon dioxide into formic acid reported so far by at least one order of magnitude when comparing production rates to the catalysts based on different metal catechols and metal-oxo clusters, as well as Cu, Mn, Rh or Ru-polypyridyl complexes independently of the nature of the host (MOFs, porous organic polymers, graphitic carbon nitride, semiconductor, Table S8).^{9,50-56} For those catalysts, production rates of up to 4 mmol_{formic acid}/g_{cat}/h were reported (Table S8), while **HRh-CPP** reaches 76 mmol_{formic acid}/g_{cat}/h. Here we note that lower catalytic activities were observed for the MOP-based catalysts when the solar simulator was replaced by a 200 W Hg lamp as light source (Table S7), similar to the setup used in literature.^{9,50-53} However, they still outperform the best heterogeneous catalysts, a porous polymer embedding a Cp*Rh(bpy) molecular complex (Cp*Rh@BpyMP-1), reported so far for the CO₂-to-formate photoreduction,⁹ by one order of magnitude, even when studied under identical conditions (Tables S7 & S8).

Thermodynamic driving force. The huge advance in production rate cannot only be attributed to the higher density of active sites in the Rh-MOPs, as the *TOF* is also at least doubled. Recently, Fontecave and co-workers demonstrated that the redox potential of the active site in a series of [Cp*Rh(X-bpy)]²⁺ catalysts correlates directly with the Hammett constant of the substituent X on the bipyridine ligand,⁵⁷ and is thus a suitable descriptor for the change in electron density on the active site and subsequently in the catalytic activity. They observed that a lower redox potential, corresponding to a higher LUMO energy position, give rise to a higher catalytic activity, which they attributed, using DFT calculations, to a lower transition state barrier of the rate-limiting step. To elucidate the origin of the differences in catalytic activity, we determined the redox potential of the active site for molecular cluster models, e.g. the **C₁₂Rh-MOP**, **C₁₂Rh-MOP_{bnix}** and **HRh-MOP_{bnix}** as soluble model catalyst for our systems, and ([([5,5'-bis(phenylethynylene)-2,2'-bipyridine](pentamethyl-cyclopentadienyl)rhodium] dichloride (Cp*Rh(bpe-bpy)Cl₂) as a soluble model catalyst for Cp*Rh@BpyMP-1. The Cp*Rh(bpe-bpy)Cl₂ molecular cluster model has been demonstrated to have the same electron density

and thus the same catalytic activity as the corresponding heterogeneous catalyst.⁹ Here we note that a molecular cluster model, which could reliably describe the electronic withdrawing effect of the additional metal carboxylate acting as substituent on the linker moiety, is not available.⁹

The electrochemical properties of the molecular cluster models were explored with cyclic voltammetry (for experimental details see SI, section 5). The cyclic voltammogram of **C₁₂Rh-MOP** indicates that the oxidation of the Rh₂ paddlewheel is reversible and occurs at approx. 0.64 V vs ferrocene/ferrocenium (Fc⁺⁰, -5.6 eV, Figure 3a, Figure S21b). Upon addition of 12 equiv. bnix to simulate the linker surrounding the MOP in the solid materials,³⁷ the redox potential of the Rh₂^{II,II}/Rh₂^{II,III} redox

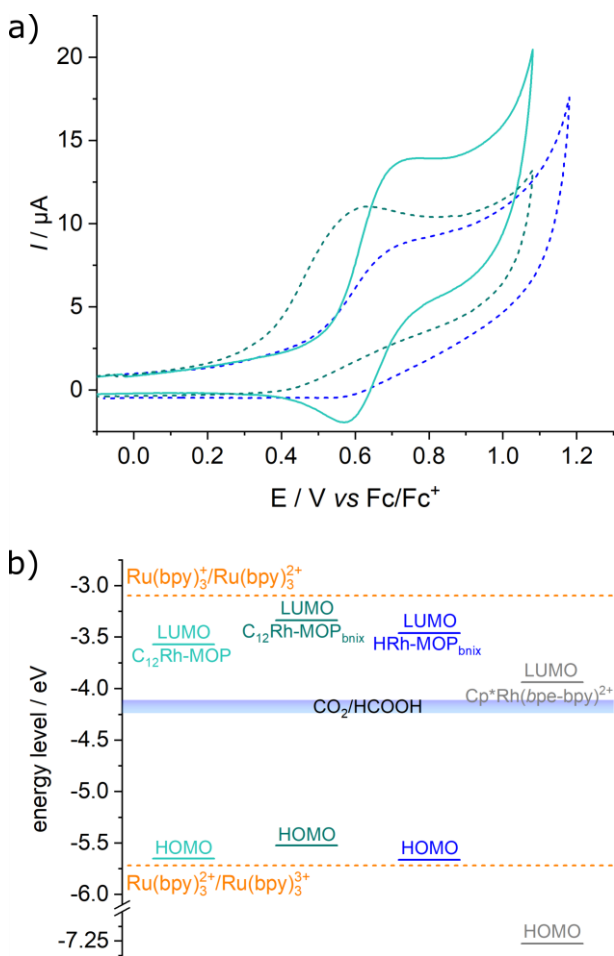


Figure 3. a) Cyclic voltammogram of **C₁₂Rh-MOP** (light turquoise), **C₁₂Rh-MOP_{bnix}** (dark turquoise) and **HRh-MOP_{bnix}** (blue) in DMF containing 0.1 M Bu₄NPF₆ using a glassy carbon working electrode at a scan rate of 100 mV·s⁻¹. b) Diagram of HOMO and LUMO energy levels of **C₁₂Rh-MOP** (light turquoise), **C₁₂Rh-MOP_{bnix}** (dark turquoise), **HRh-MOP_{bnix}** (blue) and Cp*Rh(bpe-bpy)²⁺ (gray) together with redox potentials in eV for formic acid production in acetonitrile (taking also the solvation effect of TEOA and its pK_a into account to calculate the appropriate potential range).

couple in **C₁₂Rh-MOP_{bnix}** is shifted to approx. 0.52 V vs Fc⁺⁰ (-5.5 eV) and the oxidation becomes irreversible. This shift in redox potential was further supported by differential pulse voltammetry and is similarly observed for Rh₂(OAc)₄ (Figure S21). As the reduction of the Rh species cannot be detected by cyclic voltammetry,¹⁰ we used the position of the π* → σ* transition of

the Rh-Rh bond, determined from UV-vis spectroscopy (Figure S23). The LUMO energy level of the Rh-paddlewheel are estimated to be -3.5 and -3.3 eV for **C₁₂Rh-MOP** and **C₁₂Rh-MOP_{bnix}**, respectively (Figure 3b). For the **HRh-MOP_{bnix}** molecular cluster model the LUMO position is at approx. -3.4 eV.

Although we are aware that this procedure may overestimate the HOMO-LUMO-gap and thus place the estimated LUMO position at a higher energy position, we attempted to align frontier orbital positions with respect to the redox potential of the CO₂-to-formic acid transformation, to get insights into the thermodynamic driving forces. For the Cp*Rh(*bpe*-bpy)Cl₂ molecular clusters model, the cyclic voltammogram shows a reversible signal for the two electron reduction of the Rh^{III/I} redox couple at approx. -1.06 V vs Fc⁺⁰ (-3.9 eV), corresponding to its LUMO position (HOMO-LUMO gap approx. 3.3 eV⁵⁸).

The higher LUMO position of the **C₁₂Rh-MOP_{bnix}** (-3.3 eV) as compared to the LUMO position of the **HRh-MOP_{bnix}** (-3.4 eV) is indicative of a higher electron density on Rh atoms in the Rh₂^{II,II} paddlewheel, which explains the increased catalytic activity. The Cp*Rh(*bpe*-bpy)Cl₂ molecular cluster model shows the lowest LUMO position explaining also the lowest catalytic activity observed here, with *TOFs* up to 47 h⁻¹ as compared to 58 h⁻¹ for **C₁₂Rh-MOP_{bnix}** (Table S6, entries 2, 34).⁵⁷

The redox potential of CO₂/HCOOH was calculated in acetonitrile following the procedure proposed by Mayer and co-workers⁵⁹ to be approx. 0.07 V vs Fc⁺⁰ (-5.05 eV, see SI).^{59,60} Note that acetonitrile is an aprotic solvent, thus formic acid and not formate is the main product as the p*K_a* (20.9^{61,62}) of formic acid is significantly higher than the p*K_a* of TEOAH⁺ (calculated between 15.9⁶³ and 13.7⁶⁴), which will be mainly deprotonated. We also considered the solvation and interaction of formic acid with triethanolamine using the following equation:

$$E_{\text{CO}_2(\text{g})/\text{HCO}_2\text{H}(\text{ACN})}^{\circ} = 0.07 \text{ V} - 0.059 \cdot \text{p}K_{\text{a}},^{61}$$

resulting in a redox potential range for CO₂/HCO₂H in ACN/TEOA between -4.10 and -4.24 eV. The thermodynamic driving force can be estimated from the energy difference ΔE between the redox potential $E_{\text{CO}_2(\text{g})/\text{HCO}_2\text{H}(\text{ACN})}^{\circ}$ and the LUMO position of the molecular cluster model.⁶⁵ For the molecular model systems **HRh-MOP_{bnix}**, **C₁₂Rh-MOP** and **C₁₂Rh-MOP_{bnix}**, with LUMO positions at -3.4, -3.5 and -3.3 eV, the thermodynamic driving forces for CO₂ to formic acid reduction are approximately 670, 560 and 790 meV, respectively, while the driving force is reduced to 180 meV in case of Cp*Rh(*bpe*-bpy)Cl₂ (Figure 3b). Thus, by increasing the electron density on the Rh paddlewheel, *bnix* coordination results in a higher thermodynamic driving force for the reaction, most likely by a reduced energy barrier for the rate-limiting step,⁵⁷ explaining the observed higher catalytic activities in **C₁₂Rh-CPP** and **C₁₂Rh-SAG** materials (Figure S25). This finding is in line with our recent work on molecular catalysts in microporous materials and the design of the catalytic activity by tailoring the Hammett constants of the metal ligands and subsequently the electron density on the active metal site.⁹

Recycling experiments. Recycling tests were conducted using the most active heterogeneous catalyst **C₁₂Rh-CPP** to demonstrate the heterogeneous nature of the catalyst. After 2 h of photocatalysis, the catalyst was isolated, washed, dried under vacuum and used for up to 4 cycles (Figure 4, Table S6, entries 20 – 23, see SI for further details). The catalytic activity seemingly increased slightly, but the variation is within the standard deviation and is therefore assumed to be constant. In addition,

long term experiments were carried out to understand the stability of the catalyst during several hours of continuous irradiation. After two hours of catalysis, the catalytic activity started to decrease from ~53 h⁻¹ to ~22 h⁻¹ after 8 hours of catalysis (Table S6 entries 4 – 7). The initial level of catalytic activity could be recovered by adding fresh solution of Ru(bpy)₃Cl₂ after 2, 4 and 6 hours of catalysis (Figure 4b, see SI section 6.1 for further details, Table S6 entries 8 – 19).^{53,66} Note that the deactivation of Ru(bpy)₃-based photosensitizers has even been reported after its encapsulation in a porous framework.^{67–70} However, for the **C₁₂Rh-CPP**-based photosystem, the initial catalytic activity could be retained if at least the initial molar amount of Ru(bpy)₃Cl₂ was added after each step, indicating that most of the photosensitizer was decomposed within two hours. Thus, both recycling and long-term experiments highlight the stable catalytic activity.

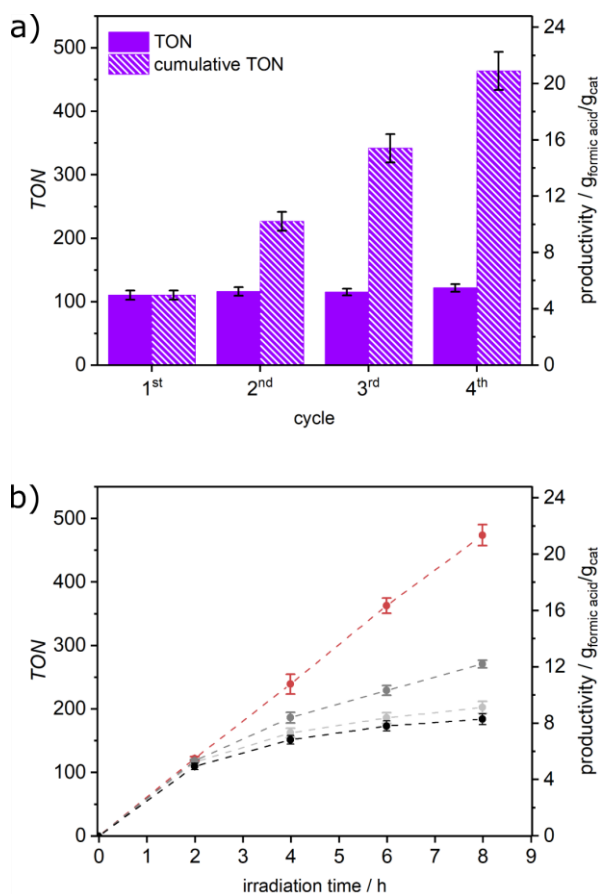


Figure 4. a) Catalytic activity over four cycles of catalysis using **C₁₂Rh-CPP** (~1.1 μmol) in the presence of Ru(bpy)₃Cl₂ (21.2 μmol, 1 equiv) as photosensitizer in ACN / TEOA (4 : 1, *V* : *V*), 2h. After each run the solid was isolated by centrifugation, washed and reused with a fresh solution of Ru(bpy)₃Cl₂. b) Comparison of TON and productivity for continuous photocatalytic experiments where different amounts of Ru(bpy)₃Cl₂ were added after 2, 4 and 6 h. 0 equiv. (black), 0.025 equiv (light grey), 0.25 equiv (grey) and 1 equiv of the initial amount of Ru(bpy)₃Cl₂ added.

Importantly, the structural properties of fresh and spent **C₁₂Rh-CPP** remain unchanged (Figure 5, and SI section 6.2). TEM analysis indicate no change of the particle morphology (Figure 5a, b). The powder X-ray diffraction (PXRD) patterns of fresh and spent catalyst are not distinguishable, featuring

broad peaks at low diffraction angles, indicative of a partial long-range ordering in the materials (Figure 5c). Importantly no changes in the relative signal intensities and full width at half maximum are observed, excluding any loss in crystallinity or amorphization to occur during catalysis. Also, no changes in the total pore volume and shape of the isotherms are observed in acetonitrile physisorption experiments of the spent heterogeneous catalysts compared to the fresh material (**C₁₂Rh-CPP**, **C₁₂Rh-SAG** and **HRh-CPP**, Figure S31), demonstrating their high framework stability. XPS spectra after one cycle of photocatalysis reveal no changes of the organic backbone of the material but significant changes of the electron binding energy on the catalytically active Rh sites (Figure 5d). After catalysis, the main signal (~75% of surface species) is centred at 309 eV with a minor contribution from reduced species (~25% of surface species) visible as a small shoulder at 307.4 eV, which might be attributed to a reduced Rh⁰ or Rh^I species (see Table S2).^{71–73} A reduction into crystalline metallic Rh is excluded by PXRD, as no additional peaks are observed after catalysis (Figure 5c) and no Rh nanoparticles are observed by TEM analysis (Figure 5a, b, Figures S24, S25). However, the formation of amorphous or tiny Rh⁰ clusters or nanoparticles cannot be excluded from PXRD and TEM analysis alone.

PDF analysis and molecular structure of the active site.

To obtain insights into the precise molecular ordering around the active site after MOP incorporation into the supramolecular polymers, we performed pair distribution function analysis (PDF).^{74–79} PDF provides local structural information such as inter-atomic distances between atoms even from amorphous materials,⁸⁰ and has been recently shown to be a powerful technique to assess the post-catalytic structural integrity of molecu-

lar components of complex catalysts.⁵³ Hence, we aimed to reveal possible structural changes after catalysis, as well as the nature of the Rh⁰ species observed by XPS analysis (Figure 5d). Interestingly, the PDFs of fresh and spent **C₁₂Rh-CPP** and **C₁₂Rh-SAG** catalysts display similar features up to 22 Å, with only slight differences in peak position and intensity (SI section S4, Figure S18). We here focus on the short distances up to 11 Å (Figure 5e, f). The peak at approx. 1.5 Å can be attributed to C-C bonds. Experimental peaks at higher distances were assigned using calculated PDF from the single crystal structure of the pristine **HRh-MOP** (assignment details in SI section S4, Figure S19b).³⁸ Peaks at 2.0 and 2.39 Å can be attributed to Rh-O and Rh-Rh distances within one paddlewheel, respectively. The diffusion factor of rhodium being stronger than those of other involved atoms of Rh-MOPs, most of the peaks seen here emanate from Rh-based pairs (distances between carbons atoms across several C-C bonds are hidden). Peaks in the region 2.9 – 7 Å can thus be assigned to distances between one Rh atom and one C or O atom from the BDC ligands within the Rh₂ paddlewheel unit, while peaks between 7.9 and 10.7 Å can be assigned to Rh-Rh distances between two neighbouring paddle wheel units in the cuboctahedral architecture. The similarity of the pristine and spent *G(r)* curves demonstrates that at the molecular level, no decomposition or distortion of the active Rh paddlewheel sites occurs after catalysis for **C₁₂Rh-CPP** and **C₁₂Rh-SAG**. This stability during catalysis is also highlighted by the clear absence of peaks at 2.7 Å, characteristic for the Rh-Rh interatomic distance in a Rh⁰ cluster.^{81,82} Also, the second most intense peak of a hypothetical Rh⁰ cluster at 4.66 Å is missing in the experimental PDF pattern (Figure S20b). The absence of those peaks (2.7 and 4.66 Å) belonging to interatomic distances within a Rh⁰ cluster thus demonstrates that no such Rh⁰ clusters are formed.

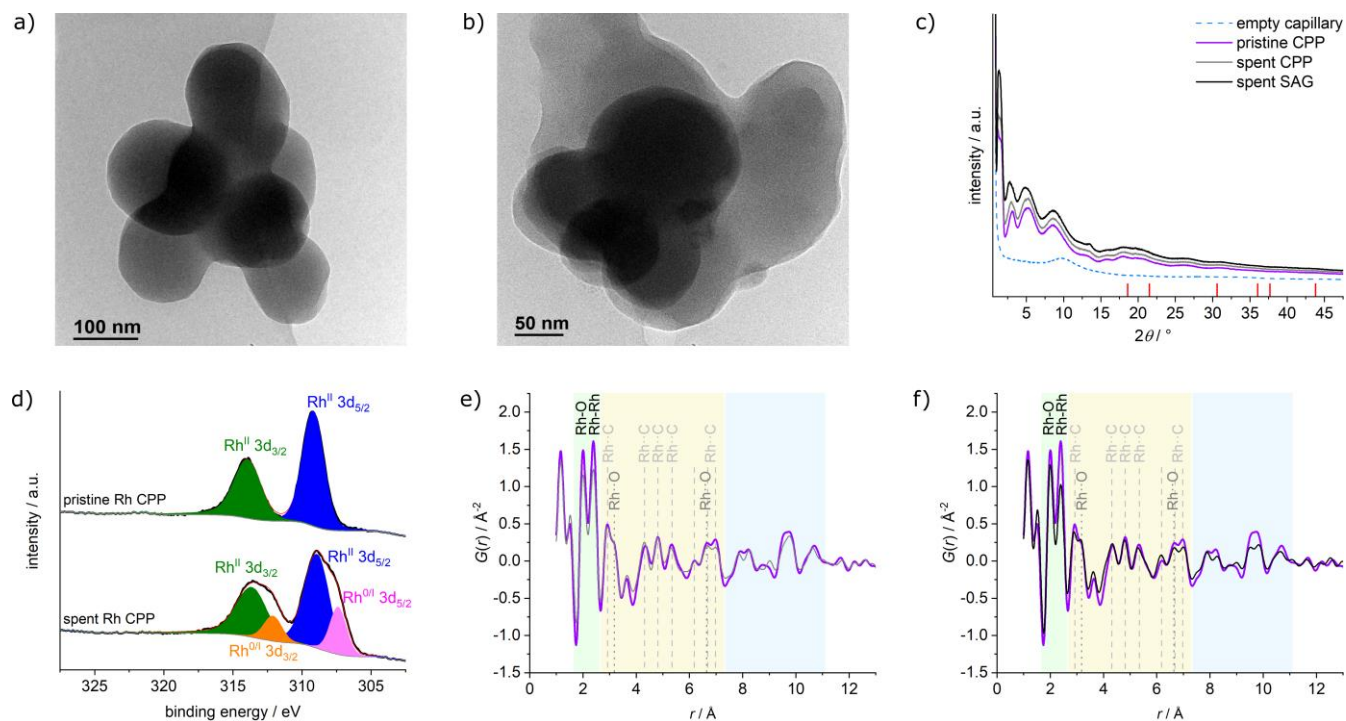


Figure 5. TEM image of a) fresh and b) spent C₁₂Rh-CPP. c) Powder XRD pattern of pristine C₁₂Rh-CPP (purple), spent C₁₂Rh-CPP catalyst (gray) and spent C₁₂Rh-SAG catalyst (black) measured using Mo K_α radiation. Bragg marker: Rh (red), COD 9008482, calculated for Mo K_α radiation. d) XPS spectra of fresh and spent catalyst including deconvolution of the signals. On the surface, 25% of the Rh atoms are reduced to a Rh^{0/I} species. e) PDF analysis: G(r) curve of pristine C₁₂Rh-CPP (purple) and spent C₁₂Rh-CPP catalyst (grey) and f) G(r)

curve PDF of pristine **C₁₂Rh-CPP** (purple) and spent **C₁₂Rh-SAG** catalyst (black). Interatomic distances within the Rh₂O₈-moiety are highlighted in green, within the Rh₂ paddlewheel unit and including the benzene dicarboxylic acid (bdc) ligands in yellow and neighboring paddlewheels in blue.

In summary, the combined XPS and PDF investigation of spent catalysts exclude any degradation into Rh⁰ clusters or particles,⁸³ or into unimolecular or polymeric Rh^I species,⁸⁴⁻⁸⁶ which, in contrast, was observed in the case of photocatalysis with [Rh₂(OAc)₄] as catalyst (Figure S29b) and has been reported for different molecular Rh₂^{II,II} carboxylates.⁸³⁻⁸⁶ Thus the fixation of the Rh₂ paddlewheel into a rigid scaffold prevents these undesired side reactions.¹⁶ In other words, the Rh-MOP structure remain the same upon catalysis, and the most reduced Rh atoms detected by XPS remain at the same positions, part of the Rh-MOP structure. Thus, this XPS signal may be attributed to a Rh^I species⁷³ either in a [Rh^IRh^{III}] or a [Rh^IRh^I] state steaming from the catalytic cycle (Figure S35), in line with oxidation states observed during the catalytic cycles of [Rh^{II}Rh^{II}] tetracarboxylate based catalysts.^{87,88} Moreover, X-ray fluorescence spectroscopy and inductively coupled plasma – optical emission spectrometry (ICP OES) analysis of the supernatant confirms that no quantifiable leaching of Rh occurs (< 5 ppm). The high stability of the Rh-MOP based materials in ACN/TEOA mixtures is in line with their reported stability towards aqueous solutions⁴⁰ and organic solvents such as dichloromethane, *N,N*-dimethylformamide or tetrahydrofuran as well as basic organic mixtures, even at elevated temperatures.^{37,44,89}

Catalytic cycle. To shine light onto the photo-induced activation of Rh₂^{II,II} paddlewheel, EPR studies under illumination were conducted on the molecular Rh-MOPs in the presence of Ru(bpy)₃Cl₂. Upon irradiation of a solution of [Ru^{II}(bpy)₃]²⁺ in ACN/TEOA mixture, the photo-excited [Ru^{II}(bpy)₃]^{2+*} is reductively quenched by reaction with TEOA yielding the [Ru^{II}(bpy)₃]^{+*} radical cation with the characteristic EPR signal at approx. *g* = 2.00 for a bipyridine centred radical (Figure S34). The signal of the reduced radical [Ru^{II}(bpy)₃]^{+*} species is efficiently quenched upon addition of Rh-MOP to the solution (Figure S34). No signal of a reduced Rh₂^{II,I} paddlewheel species can be observed with *g*-values well above 2,^{83,86,90} in line with the electrochemical investigations (Figure 3). Combining the results from XPS, EPR and electro chemical characterization, we postulate a reaction mechanism that involves (i) the photo-excitation and reductive quenching of the [Ru^{II}(bpy)₃]²⁺ photosensitizer by TEOA to yield [Ru^{II}(bpy)₃]^{+*}, then (ii) electron transfer from the reduced photosensitizer [Ru^{II}(bpy)₃]^{+*} to the Rh catalyst and followed by (iii) the reduction of CO₂ into formic acid (Figure S35).^{11,66,91} The required protons for the formic acid formation most likely stem from proton abstraction from the nitrogen centred TEOA^{+*} radical to yield a carbon centred radical, which is a much stronger reductant, capable of transferring a second electron as well as a second proton and thus avoiding back electron transfer.^{36,92,93}

CONCLUSION

We investigated Rh₂ paddlewheel-based cuboctahedral metal-organic polyhedra, Rh-MOP, both molecularly and self-assembled into supramolecular polymers colloidal particle (Rh-CPP) and colloidal aerogel (Rh-SAG) as well as [Rh₃BTC₂]_n (Rh-MOF) for photocatalytic CO₂ reduction. The heterogenized supramolecular catalysts showed high turnover frequencies of up to 60 h⁻¹, corresponding to production rates of approx. 2.7 g_{formic acid}/g_{cat}/h, outperforming the molecular Rh-MOP catalysts by up to 30 % and state-of-the-art heterogeneous photocatalytic systems, including Rh-MOF, by at least a factor of twelve. The

very high catalytic activity compared to other heterogeneous photocatalytic systems can be rationalized by the high number of Rh sites per gram of catalyst, but also by their very high accessibility inside the supramolecular cage. The accessibility of the cage inside the supramolecular polymers for the solvent in liquid phase catalysis was demonstrated using acetonitrile vapour physisorption. All materials show high acetonitrile uptake while nitrogen physisorption experiments at 77 K proved to be unsuitable for the evaluation of the accessibility and porosity in liquid phase catalysis.

Importantly, we were able to show, by pair distribution function analysis, that all Rh is coordinated in molecular cages and that no formation of colloidal Rh⁰ or Rh nanoparticles occurs, indicating the high stability of these heterogeneous catalysts. This is confirmed by recycling tests of at least 4 cycles without any loss of activity. The coordination of the MOP by electron-donating N-ligands not only leads to a heterogenization of the active centre in a stable, and easily recyclable polymer. XPS spectroscopy and electrochemical characterization also show that the N-ligands increases the electron density at the active Rh site compared to the molecular MOP catalyst in solution, leading to a higher thermodynamic driving force of the reaction. This finding is in line with our recent works on molecular catalysts in microporous materials and the design of the catalytic activity by tailoring the Hammett constants of the metal ligands.

The present work demonstrates the high potential of MOP and of their polymer derivatives as catalysts for the photoreduction of CO₂ with unprecedented efficiency and opens new perspectives for the electronic design of novel discrete molecular architectures with accessible metal sites for the production of solar fuels.

ASSOCIATED CONTENT

Supporting Information. Detailed experimental procedures, materials and instruments used as well as additional material characterization and overview are provided in the Supporting Information. This material is available free of charge via the Internet at <http://pubs.acs.org>.

AUTHOR INFORMATION

Corresponding Author

* florian.wisser@ur.de, jerome.canivet@ircelyon.univ-lyon1.fr, shuheif.furukawa@icems.kyoto-u.ac.jp

ORCID

Ashta C. Ghosh: 0000-0003-3137-6580
 Alexandre Legrand: 0000-0002-7975-9348
 Gavin A. Craig: 0000-0003-3542-4850
 Capucine Sassoie: 0000-0003-2790-888X
 Gábor Balázs: 0000-0003-3497-7082
 David Farrusseng: 0000-0002-9093-4143
 Shuheif Furukawa: 0000-0003-3849-8038
 Jérôme Canivet: 0000-0002-0458-3085
 Florian M. Wisser: 0000-0002-5925-895X

Present Addresses

♦ University of Strathclyde, Department of Pure and Applied Chemistry.

Author Contributions

^Δ A.C.G. and A.L. contributed equally. The manuscript was written through contributions of all authors. All authors have given approval to the final version of the manuscript.

ACKNOWLEDGMENT

The authors are grateful to Caroline Mellot-Draznieks for fruitful discussion of PDF data. F.M.W. gratefully acknowledges financial support from the Deutsche Forschungsgemeinschaft (DFG, grant number WI 4721/3-1). F.M.W. and A.C.G. acknowledge financial support from CNRS through Momentum 2018 excellence grant. D.F., J.C., S.F. and A.L. acknowledge financial support from the CNRS International Research Project “Small Molecule Lab: IRP-Smolab” and IDEX of Lyon University. This study was supported by JSPS KAKENHI Grant Number 20K15366 (Wakate) for A.L. and 19H04575 (Coordination Asymmetry) and 18H01995 (Kiban B) for S.F. The authors thank the iCeMS Analysis Center for access to analytical instruments. The authors are very grateful to H. Izu for the access to the electrochemistry device, P. Mascunan for ICP-OES, N. Bonnet for XRF analysis, P. P. Bargiela for XPS analysis and Z. Shahin for TEM analysis.

REFERENCES

- Cui, X.; Li, W.; Ryabchuk, P.; Junge, K.; Beller, M. Bridging Homogeneous and Heterogeneous Catalysis by Heterogeneous Single-Metal-Site Catalysts. *Nat. Catal.* **2018**, *1* (6), 385–397. <https://doi.org/10.1038/s41929-018-0090-9>.
- Drake, T.; Ji, P.; Lin, W. Site Isolation in Metal–Organic Frameworks Enables Novel Transition Metal Catalysis. *Acc. Chem. Res.* **2018**, *51* (9), 2129–2138. <https://doi.org/10.1021/acs.accounts.8b00297>.
- Copéret, C.; Comas-Vives, A.; Conley, M. P.; Estes, D. P.; Fedorov, A.; Mougél, V.; Nagae, H.; Núñez-Zarur, F.; Zhizhko, P. A. Surface Organometallic and Coordination Chemistry toward Single-Site Heterogeneous Catalysts: Strategies, Methods, Structures, and Activities. *Chem. Rev.* **2016**, *116* (2), 323–421. <https://doi.org/10.1021/acs.chemrev.5b00373>.
- Copéret, C.; Fedorov, A.; Zhizhko, P. A. Surface Organometallic Chemistry: Paving the Way Beyond Well-Defined Supported Organometallics and Single-Site Catalysis. *Catal. Letters* **2017**, *147* (9), 2247–2259. <https://doi.org/10.1007/s10562-017-2107-4>.
- Wisser, F. M.; Mohr, Y.; Quadrelli, E. A.; Canivet, J. Porous Macroligands: Materials for Heterogeneous Molecular Catalysis. *ChemCatChem* **2020**, *12* (5), 1270–1275. <https://doi.org/10.1002/cctc.201902064>.
- Qiao, B.; Wang, A.; Yang, X.; Allard, L. F.; Jiang, Z.; Cui, Y.; Liu, J.; Li, J.; Zhang, T. Single-Atom Catalysis of CO Oxidation Using Pt/FeOx. *Nat. Chem.* **2011**, *3* (8), 634–641. <https://doi.org/10.1038/nchem.1095>.
- Quadrelli, E. A.; Basset, J.-M. On Silsesquioxanes' Accuracy as Molecular Models for Silica-Grafted Complexes in Heterogeneous Catalysis. *Coord. Chem. Rev.* **2010**, *254* (5–6), 707–728. <https://doi.org/10.1016/j.ccr.2009.09.031>.
- Conley, M. P.; Copéret, C. State of the Art and Perspectives in the “Molecular Approach” towards Well-Defined Heterogeneous Catalysts. *Top. Catal.* **2014**, *57* (10–13), 843–851. <https://doi.org/10.1007/s11244-014-0245-0>.
- Wisser, F. M.; Berruyer, P.; Cardenas, L.; Mohr, Y.; Quadrelli, E. A.; Lesage, A.; Farrusseng, D.; Canivet, J. Hammett Parameter in Microporous Solids as Macroligands for Heterogenized Photocatalysts. *ACS Catal.* **2018**, *8* (3), 1653–1661. <https://doi.org/10.1021/acscatal.7b03998>.
- Chinapang, P.; Okamura, M.; Itoh, T.; Kondo, M.; Masaoka, S. Development of a Framework Catalyst for Photocatalytic Hydrogen Evolution. *Chem. Commun.* **2018**, *54* (10), 1174–1177. <https://doi.org/10.1039/C7CC08013A>.
- Lin, S.; Turro, C. Dirhodium Complexes as Panchromatic Sensitizers, Electrocatalysts, and Photocatalysts. *Chem. – A Eur. J.* **2021**, *27* (17), 5379–5387. <https://doi.org/10.1002/chem.202003950>.
- Kumar, D. K.; Filatov, A. S.; Napier, M.; Sun, J.; Dikarev, E. V.; Petrukina, M. A. Dirhodium Paddlewheel with Functionalized Carboxylate Bridges: New Building Block for Self-Assembly and Immobilization on Solid Support. *Inorg. Chem.* **2012**, *51* (8), 4855–4861. <https://doi.org/10.1021/ic300382j>.
- Liu, J.; Fasel, C.; Braga-Groszewicz, P.; Rothermel, N.; Lilly Thankamony, A. S.; Sauer, G.; Xu, Y.; Gutmann, T.; Buntkowsky, G. Heterogeneous Self-Supported Dirhodium(II) Catalysts with High Catalytic Efficiency in Cyclopropanation—a Structural Study. *Catal. Sci. Technol.* **2016**, *6* (21), 7830–7840. <https://doi.org/10.1039/C6CY00915H>.
- Mori, W.; Takamizawa, S.; Kato, C. N.; Ohmura, T.; Sato, T. Molecular-Level Design of Efficient Microporous Materials Containing Metal Carboxylates: Inclusion Complex Formation with Organic Polymer, Gas-Occlusion Properties, and Catalytic Activities for Hydrogenation of Olefins. *Microporous Mesoporous Mater.* **2004**, *73* (1–2), 31–46. <https://doi.org/10.1016/j.micromeso.2004.02.019>.
- SATO, T.; MORI, W.; KATO, C.; YANAOKA, E.; KURIBAYASHI, T.; OHTERA, R.; SHIRAIISHI, Y. Novel Microporous Rhodium(II) Carboxylate Polymer Complexes Containing Metalloporphyrin: Syntheses and Catalytic Performances in Hydrogenation of Olefins. *J. Catal.* **2005**, *232* (1), 186–198. <https://doi.org/10.1016/j.jcat.2005.02.007>.
- Shakya, D. M.; Ejegebawo, O. A.; Rajeshkumar, T.; Senanayake, S. D.; Brandt, A. J.; Farzandh, S.; Acharya, N.; Ebrahim, A. M.; Frenkel, A. I.; Rui, N.; Tate, G. L.; Monnier, J. R.; Vogiatzis, K. D.; Shustova, N. B.; Chen, D. A. Selective Catalytic Chemistry at Rhodium(II) Nodes in Bimetallic Metal–Organic Frameworks. *Angew. Chemie - Int. Ed.* **2019**, *58* (46), 16533–16537. <https://doi.org/10.1002/anie.201908761>.
- Nickerl, G.; Stoeck, U.; Burkhardt, U.; Senkovska, I.; Kaskel, S. A Catalytically Active Porous Coordination Polymer Based on a Dinuclear Rhodium Paddle-Wheel Unit. *J. Mater. Chem. A* **2014**, *2* (1), 144–148. <https://doi.org/10.1039/C3TA12795H>.
- Heinz, W. R.; Agirrezabal-Telleria, I.; Junk, R.; Berger, J.; Wang, J.; Sharapa, D. I.; Gil-Calvo, M.; Luz, I.; Soukri, M.; Studt, F.; Wang, Y.; Wöll, C.; Bunzen, H.; Drees, M.; Fischer, R. A. Thermal Defect Engineering of Precious Group Metal–Organic Frameworks: A Case Study on Ru/Rh-HKUST-1 Analogues. *ACS Appl. Mater. Interfaces* **2020**, *12* (36), 40635–40647. <https://doi.org/10.1021/acsami.0c10721>.
- Stoll, T.; Castillo, C. E.; Kayanuma, M.; Sandroni, M.; Daniel, C.; Odobel, F.; Fortage, J.; Collomb, M.-N. Photo-Induced Redox Catalysis for Proton Reduction to Hydrogen with Homogeneous Molecular Systems Using Rhodium-Based Catalysts. *Coord. Chem. Rev.* **2015**, *304–305*, 20–37. <https://doi.org/10.1016/j.ccr.2015.02.002>.
- Kataoka, Y.; Sato, K.; Miyazaki, Y.; Suzuki, Y.; Tanaka, H.; Kitagawa, Y.; Kawakami, T.; Okumura, M.; Mori, W. Photocatalytic Hydrogen Production from Water Using Heterogeneous Two-Dimensional Rhodium Coordination Polymer [Rh₂(p-BDC)₂]·n. *N. Chem. Lett.* **2010**, *39* (4), 358–359. <https://doi.org/10.1246/cl.2010.358>.
- Bavykina, A.; Cadiau, A.; Gascon, J. Porous Liquids Based on Porous Cages, Metal Organic Frameworks and Metal Organic Polyhedra. *Coord. Chem. Rev.* **2019**, *386*, 85–95. <https://doi.org/10.1016/j.ccr.2019.01.015>.
- Hasell, T.; Schmidtman, M.; Cooper, A. I. Molecular Doping of Porous Organic Cages. *J. Am. Chem. Soc.* **2011**, *133* (38), 14920–14923. <https://doi.org/10.1021/ja205969q>.
- Sharma, V.; De, D.; Saha, R.; Chattaraj, P. K.; Bharadwaj, P. K. Flexibility Induced Encapsulation of Ultrafine Palladium Nanoparticles into Organic Cages for Tsuji–Trost Allylation. *ACS Appl. Mater. Interfaces* **2020**, *12* (7), 8539–8546. <https://doi.org/10.1021/acscami.9b19480>.
- Vardhan, H.; Yusubov, M.; Verpoort, F. Self-Assembled Metal–Organic Polyhedra: An Overview of Various Applications. *Coord. Chem. Rev.* **2016**, *306* (P1), 171–194. <https://doi.org/10.1016/j.ccr.2015.05.016>.
- Dechnik, J.; Gascon, J.; Doonan, C. J.; Janiak, C.; Sumbly, C. J. Mixed-Matrix Membranes. *Angew. Chemie - Int. Ed.* **2017**, *56* (32), 9292–9310. <https://doi.org/10.1002/anie.201701109>.
- Hosono, N.; Kitagawa, S. Modular Design of Porous Soft Materials via Self-Organization of Metal–Organic Cages. *Acc. Chem. Res.* **2018**, *51* (10), 2437–2446. <https://doi.org/10.1021/acs.accounts.8b00361>.
- Gosselin, A. J.; Rowland, C. A.; Bloch, E. D. Permanently

- Microporous Metal–Organic Polyhedra. *Chem. Rev.* **2020**, *120* (16), 8987–9014. <https://doi.org/10.1021/acs.chemrev.9b00803>.
- (28) Vardhan, H.; Verpoort, F. Metal–Organic Polyhedra: Catalysis and Reactive Intermediates. *Adv. Synth. Catal.* **2015**, *357* (7), 1351–1368. <https://doi.org/10.1002/adsc.201400778>.
- (29) Tan, C.; Jiao, J.; Li, Z.; Liu, Y.; Han, X.; Cui, Y. Design and Assembly of a Chiral Metallosalen-Based Octahedral Coordination Cage for Supramolecular Asymmetric Catalysis. *Angew. Chemie Int. Ed.* **2018**, *57* (8), 2085–2090. <https://doi.org/10.1002/anie.201711310>.
- (30) Lee, H. S.; Jee, S.; Kim, R.; Bui, H.-T.; Kim, B.; Kim, J.-K.; Park, K. S.; Choi, W.; Kim, W.; Choi, K. M. A Highly Active, Robust Photocatalyst Heterogenized in Discrete Cages of Metal–Organic Polyhedra for CO₂ Reduction. *Energy Environ. Sci.* **2020**, *13* (2), 519–526. <https://doi.org/10.1039/C9EE02619C>.
- (31) Lee, S.; Jeong, H.; Nam, D.; Lah, M. S.; Choe, W. The Rise of Metal–Organic Polyhedra. *Chem. Soc. Rev.* **2021**, *50* (1), 528–555. <https://doi.org/10.1039/D0CS00443J>.
- (32) Ji, C.; Wang, W.; El-Sayed, E.-S. M.; Liu, G.; Si, Y.; Su, K.; Ju, Z.; Wu, F.; Yuan, D. A High-Efficiency Dye-Sensitized Pt(II) Decorated Metal–Organic Cage for Visible-Light-Driven Hydrogen Production. *Appl. Catal. B Environ.* **2021**, *285*, 119782. <https://doi.org/10.1016/j.apcatb.2020.119782>.
- (33) Chen, L.; Yang, T.; Cui, H.; Cai, T.; Zhang, L.; Su, C.-Y. A Porous Metal–Organic Cage Constructed from Rhodium Paddle-Wheels: Synthesis, Structure and Catalysis. *J. Mater. Chem. A* **2015**, *3* (40), 20201–20209. <https://doi.org/10.1039/C5TA05592J>.
- (34) Kang, Y.-H.; Liu, X.-D.; Yan, N.; Jiang, Y.; Liu, X.-Q.; Sun, L.-B.; Li, J.-R. Fabrication of Isolated Metal–Organic Polyhedra in Confined Cavities: Adsorbents/Catalysts with Unusual Dispersity and Activity. *J. Am. Chem. Soc.* **2016**, *138* (19), 6099–6102. <https://doi.org/10.1021/jacs.6b01207>.
- (35) Zhang, Z.; Lei, Y.; Zhou, J.; Cui, M.; Chen, X.; Fei, Z.; Liu, Q.; Tang, J.; Qiao, X. Simultaneous Shaping and Confinement of Metal–Organic Polyhedra in Alginate-SiO₂ Spheres. *Chem. Commun.* **2020**, *56* (94), 14833–14836. <https://doi.org/10.1039/D0CC05619G>.
- (36) Yamazaki, Y.; Takeda, H.; Ishitani, O. Photocatalytic Reduction of CO₂ Using Metal Complexes. *J. Photochem. Photobiol. C Photochem. Rev.* **2015**, *25* (4), 106–137. <https://doi.org/10.1016/j.jphotochemrev.2015.09.001>.
- (37) Carné-Sánchez, A.; Craig, G. A.; Larpent, P.; Hirose, T.; Higuchi, M.; Kitagawa, S.; Matsuda, K.; Urayama, K.; Furukawa, S. Self-Assembly of Metal–Organic Polyhedra into Supramolecular Polymers with Intrinsic Microporosity. *Nat. Commun.* **2018**, *9* (1), 2506. <https://doi.org/10.1038/s41467-018-04834-0>.
- (38) Furukawa, S.; Horike, N.; Kondo, M.; Hijikata, Y.; Carné-Sánchez, A.; Larpent, P.; Louvain, N.; Diring, S.; Sato, H.; Matsuda, R.; Kawano, R.; Kitagawa, S. Rhodium–Organic Cuboctahedra as Porous Solids with Strong Binding Sites. *Inorg. Chem.* **2016**, *55* (21), 10843–10846. <https://doi.org/10.1021/acs.inorgchem.6b02091>.
- (39) Miklitz, M.; Jelfs, K. E. Pywindow: Automated Structural Analysis of Molecular Pores. *J. Chem. Inf. Model.* **2018**, *58* (12), 2387–2391. <https://doi.org/10.1021/acs.jcim.8b00490>.
- (40) Kawano, R.; Horike, N.; Hijikata, Y.; Kondo, M.; Carné-Sánchez, A.; Larpent, P.; Ikemura, S.; Osaki, T.; Kamiya, K.; Kitagawa, S.; Takeuchi, S.; Furukawa, S. Metal–Organic Cuboctahedra for Synthetic Ion Channels with Multiple Conductance States. *Chem* **2017**, *2* (3), 393–403. <https://doi.org/10.1016/j.chempr.2017.02.002>.
- (41) Heinz, W. R.; Kratky, T.; Drees, M.; Wimmer, A.; Tomanec, O.; Günther, S.; Schuster, M.; Fischer, R. A. Mixed Precious-Group Metal–Organic Frameworks: A Case Study of the HKUST-1 Analogue [Ru_xRh_{3-x}(BTC)₂]. *Dalt. Trans.* **2019**, *48* (32), 12031–12039. <https://doi.org/10.1039/C9DT01198F>.
- (42) Chui, S. S. Y.; Lo, S. M. F.; Charmant, J. P. H.; Orpen, A. G.; Williams, I. D. A Chemically Functionalizable Nanoporous Material [Cu₃(TMA)₂(H₂O)₃](N). *Science* (80-.). **1999**, *283* (5405), 1148–1150. <https://doi.org/10.1126/science.283.5405.1148>.
- (43) Wang, Z.; Villa Santos, C.; Legrand, A.; Haase, F.; Hara, Y.; Kanamori, K.; Aoyama, T.; Urayama, K.; Doherty, C. M.; Smales, G. J.; Pauw, B. R.; Colón, Y. J.; Furukawa, S. Multiscale Structural Control of Linked Metal–Organic Polyhedra Gel by Aging-Induced Linkage-Reorganization. *Chem. Sci.* **2021**, *12* (38), 12556–12563. <https://doi.org/10.1039/D1SC02883A>.
- (44) Carné-Sánchez, A.; Craig, G. A.; Larpent, P.; Guiller, V.; Urayama, K.; Maspocho, D.; Furukawa, S. A Coordinative Solubilizer Method to Fabricate Soft Porous Materials from Insoluble Metal–Organic Polyhedra. *Angew. Chemie Int. Ed.* **2019**, *58* (19), 6347–6350. <https://doi.org/10.1002/anie.201901668>.
- (45) Itagaki, S.; Yamaguchi, K.; Mizuno, N. Catalytic Synthesis of Silyl Formates with Iatm of CO₂ and Their Utilization for Synthesis of Formyl Compounds and Formic Acid. *J. Mol. Catal. A Chem.* **2013**, *366*, 347–352. <https://doi.org/10.1016/j.molcata.2012.10.014>.
- (46) Fulmer, G. R.; Miller, A. J. M.; Sherden, N. H.; Gottlieb, H. E.; Nudelman, A.; Stoltz, B. M.; Bercaw, J. E.; Goldberg, K. I. NMR Chemical Shifts of Trace Impurities: Common Laboratory Solvents, Organics, and Gases in Deuterated Solvents Relevant to the Organometallic Chemist. *Organometallics* **2010**, *29* (9), 2176–2179. <https://doi.org/10.1021/om100106e>.
- (47) Tamaki, Y.; Koike, K.; Morimoto, T.; Ishitani, O. Substantial Improvement in the Efficiency and Durability of a Photocatalyst for Carbon Dioxide Reduction Using a Benzoimidazole Derivative as an Electron Donor. *J. Catal.* **2013**, *304*, 22–28. <https://doi.org/10.1016/j.jcat.2013.04.002>.
- (48) Hansch, C.; Leo, A.; Taft, R. W. A Survey of Hammett Substituent Constants and Resonance and Field Parameters. *Chem. Rev.* **1991**, *91* (2), 165–195. <https://doi.org/10.1021/cr00002a004>.
- (49) Vermoortele, F.; Vandichel, M.; Van de Voorde, B.; Ameloot, R.; Waroquier, M.; Van Speybroeck, V.; De Vos, D. E. Electronic Effects of Linker Substitution on Lewis Acid Catalysis with Metal–Organic Frameworks. *Angew. Chemie Int. Ed.* **2012**, *51* (20), 4887–4890. <https://doi.org/10.1002/anie.201108565>.
- (50) Lee, Y.; Kim, S.; Fei, H.; Kang, J. K.; Cohen, S. M. Photocatalytic CO₂ Reduction Using Visible Light by Metal–Monocatecholates Species in a Metal–Organic Framework. *Chem. Commun.* **2015**, *51* (92), 16549–16552. <https://doi.org/10.1039/C5CC04506A>.
- (51) Sun, D.; Gao, Y.; Fu, J.; Zeng, X.; Chen, Z.; Li, Z. Construction of a Supported Ru Complex on Bifunctional MOF-253 for Photocatalytic CO₂ Reduction under Visible Light. *Chem. Commun.* **2015**, *51* (13), 2645–2648. <https://doi.org/10.1039/C4CC09797A>.
- (52) Kajiwara, T.; Fujii, M.; Tsujimoto, M.; Kobayashi, K.; Higuchi, M.; Tanaka, K.; Kitagawa, S. Photochemical Reduction of Low Concentrations of CO₂ in a Porous Coordination Polymer with a Ruthenium(II)–CO Complex. *Angew. Chemie - Int. Ed.* **2016**, *55* (8), 2697–2700. <https://doi.org/10.1002/anie.201508941>.
- (53) Benseghir, Y.; Lemarchand, A.; Duguet, M.; Mialane, P.; Gomez-Mingot, M.; Roch-Marchal, C.; Pino, T.; Ha-Thi, M.-H.; Haouas, M.; Fontecave, M.; Dolbecq, A.; Sassoie, C.; Mellot-Draznieks, C. Co-Immobilization of a Rh Catalyst and a Keggin Polyoxometalate in the UiO-67 Zr-Based Metal–Organic Framework: In Depth Structural Characterization and Photocatalytic Properties for CO₂ Reduction. *J. Am. Chem. Soc.* **2020**, *142* (20), 9428–9438. <https://doi.org/10.1021/jacs.0c02425>.
- (54) Kuriki, R.; Matsunaga, H.; Nakashima, T.; Wada, K.; Yamakata, A.; Ishitani, O.; Maeda, K. Nature-Inspired, Highly Durable CO₂ Reduction System Consisting of a Binuclear Ruthenium(II) Complex and an Organic Semiconductor Using Visible Light. *J. Am. Chem. Soc.* **2016**, *138* (15), 5159–5170. <https://doi.org/10.1021/jacs.6b01997>.
- (55) Cauwenbergh, R.; Das, S. Photochemical Reduction of Carbon Dioxide to Formic Acid. *Green Chem.* **2021**, *23* (7), 2553–2574. <https://doi.org/10.1039/D0GC04040A>.
- (56) Woo, S.-J.; Choi, S.; Kim, S.-Y.; Kim, P. S.; Jo, J. H.; Kim, C. H.; Son, H.-J.; Pac, C.; Kang, S. O. Highly Selective and Durable Photochemical CO₂ Reduction by Molecular Mn(II) Catalyst Fixed on a Particular Dye-Sensitized TiO₂ Platform. *ACS Catal.* **2019**, *9* (3), 2580–2593. <https://doi.org/10.1021/acscatal.8b03816>.
- (57) Todorova, T. K.; Huan, T. N.; Wang, X.; Agarwala, H.; Fontecave, M. Controlling Hydrogen Evolution during

- Photoreduction of CO₂ to Formic Acid Using [Rh(R-Bpy)(Cp*)Cl] + Catalysts: A Structure–Activity Study. *Inorg. Chem.* **2019**, *58* (10), 6893–6903. <https://doi.org/10.1021/acs.inorgchem.9b00371>. (72)
- (58) Oppelt, K.; Egbe, D. A. M.; Monkowius, U.; List, M.; Zabel, M.; Sariciftci, N. S.; Knör, G. Luminescence and Spectroscopic Studies of Organometallic Rhodium and Rhenium Multichromophore Systems Carrying Polypyridyl Acceptor Sites and Phenylethynyl Antenna Subunits. *Journal of Organometallic Chemistry.* **2011**, pp 2252–2258. <https://doi.org/10.1016/j.jorganchem.2010.11.008>. (73)
- (59) Pegis, M. L.; Roberts, J. A. S.; Wasylenko, D. J.; Mader, E. A.; Appel, A. M.; Mayer, J. M. Standard Reduction Potentials for Oxygen and Carbon Dioxide Couples in Acetonitrile and N,N-Dimethylformamide. *Inorg. Chem.* **2015**, *54* (24), 11883–11888. <https://doi.org/10.1021/acs.inorgchem.5b02136>. (74)
- (60) Johnson, S. I.; Nielsen, R. J.; Goddard, W. A. Selectivity for HCO₂⁻ over H₂ in the Electrochemical Catalytic Reduction of CO₂ by (POCOP)IrH₂. *ACS Catal.* **2016**, *6* (10), 6362–6371. <https://doi.org/10.1021/acscatal.6b01755>. (75)
- (61) Waldie, K. M.; Ostericher, A. L.; Reineke, M. H.; Sasayama, A. F.; Kubiak, C. P. Hydricity of Transition-Metal Hydrides: Thermodynamic Considerations for CO₂ Reduction. *ACS Catal.* **2018**, *8* (2), 1313–1324. <https://doi.org/10.1021/acscatal.7b03396>. (76)
- (62) Stirling, M. J.; Sweeney, G.; MacRory, K.; Blacker, A. J.; Page, M. I. The Kinetics and Mechanism of the Organo-Iridium-Catalysed Enantioselective Reduction of Imines. *Org. Biomol. Chem.* **2016**, *14* (14), 3614–3622. <https://doi.org/10.1039/C6OB00245E>. (77)
- (63) Izutsu, K.; Nakamura, T.; Takizawa, K.; Takeda, A. Calorimetric Determination of Thermodynamic Parameters for the Dissociations of Acids in Dipolar Aprotic Solvents. *Bull. Chem. Soc. Jpn.* **1985**, *58* (2), 455–458. <https://doi.org/10.1246/bcsj.58.455>. (78)
- (64) Sampaio, R. N.; Grills, D. C.; Polyansky, D. E.; Szalda, D. J.; Fujita, E. Unexpected Roles of Triethanolamine in the Photochemical Reduction of CO₂ to Formate by Ruthenium Complexes. *J. Am. Chem. Soc.* **2020**, *142* (5), 2413–2428. <https://doi.org/10.1021/jacs.9b11897>. (79)
- (65) Stegbauer, L.; Zech, S.; Savasci, G.; Banerjee, T.; Podjaski, F.; Schwinghammer, K.; Ochsenfeld, C.; Lotsch, B. V. Tailor-Made Photoconductive Pyrene-Based Covalent Organic Frameworks for Visible-Light Driven Hydrogen Generation. *Adv. Energy Mater.* **2018**, *8* (24), 1–8. <https://doi.org/10.1002/aenm.201703278>. (80)
- (66) Chambers, M. B.; Wang, X.; Elgrishi, N.; Hendon, C. H.; Walsh, A.; Bonnefoy, J.; Canivet, J.; Quadrelli, E. A.; Farrusseng, D.; Mellot-Draznieks, C.; Fontecave, M. Photocatalytic Carbon Dioxide Reduction with Rhodium-Based Catalysts in Solution and Heterogenized within Metal–Organic Frameworks. *ChemSusChem* **2015**, *8* (4), 603–608. <https://doi.org/10.1002/cssc.201403345>. (81)
- (67) Wang, C.; DeKrafft, K. E.; Lin, W. Pt Nanoparticles@Photoactive Metal–Organic Frameworks: Efficient Hydrogen Evolution via Synergistic Photoexcitation and Electron Injection. *J. Am. Chem. Soc.* **2012**, *134* (17), 7211–7214. <https://doi.org/10.1021/ja300539p>. (82)
- (68) Wang, X.; Wissler, F. M.; Canivet, J.; Fontecave, M.; Mellot-Draznieks, C. Immobilization of a Full Photosystem in the Large-Pore MIL-101 Metal–Organic Framework for CO₂ Reduction. *ChemSusChem* **2018**, *11* (18), 3315–3322. <https://doi.org/10.1002/cssc.201801066>. (83)
- (69) Stanley, P. M.; Thomas, C.; Thyryhaug, E.; Urstoege, A.; Schuster, M.; Hauer, J.; Rieger, B.; Warnan, J.; Fischer, R. A. Entrapped Molecular Photocatalyst and Photosensitizer in Metal–Organic Framework Nanoreactors for Enhanced Solar CO₂ Reduction. **2021**. <https://doi.org/10.1021/acscatal.0c04673>. (84)
- (70) Stanley, P. M.; Parkulab, M.; Rieger, B.; Warnan, J.; Fischer, R. A. Understanding Entrapped Molecular Photosystem and Metal–Organic Framework Synergy for Improved Solar Fuel Production. *Faraday Discuss.* **2021**, *231*, 281–297. <https://doi.org/10.1039/D1FD00009H>. (85)
- (71) NIST X-Ray Photoelectron Spectroscopy Database, NIST Standard Reference Database Number 20, National Institute of Standards and Technology, Gaithersburg MD, 20899 (2000). [Doi:10.18434/T4T88K](https://doi.org/10.18434/T4T88K), (Retrieved 16.01.2022). (86)
- Lippi, R.; Coghlan, C. J.; Howard, S. C.; Easton, C. D.; Gu, Q.; Patel, J.; Sumbly, C. J.; Kennedy, D. F.; Doonan, C. J. In Situ MOF-Templating of Rh Nanocatalysts under Reducing Conditions. *Aust. J. Chem.* **2020**, *73* (12), 1271. <https://doi.org/10.1071/CH20193>. (87)
- Furlani, C.; Mattogno, G.; Polzonetti, G.; Sbrana, G.; Valentini, G. Surface Oxidation of Some Rh(I) Compounds and Some Polymer-Supported Rh(I) Catalysts. *J. Catal.* **1985**, *94* (2), 335–342. [https://doi.org/10.1016/0021-9517\(85\)90198-8](https://doi.org/10.1016/0021-9517(85)90198-8). (88)
- Debye, P.; Menke, H. The Determination of the Inner Structure of Liquids by X-Ray Means. *Phys. Zeitschrift* **1930**, *31*, 797–798. (89)
- Billinge, S. J. L.; Kanatzidis, M. G. Beyond Crystallography: The Study of Disorder, Nanocrystallinity and Crystallographically Challenged Materials with Pair Distribution Functions. *Chem. Commun.* **2004**, *4* (7), 749. <https://doi.org/10.1039/b309577k>. (90)
- Petkov, V. Nanostructure by High-Energy X-Ray Diffraction. *Mater. Today* **2008**, *11* (11), 28–38. [https://doi.org/10.1016/S1369-7021\(08\)70236-0](https://doi.org/10.1016/S1369-7021(08)70236-0). (91)
- Takeshi, E.; Billinge, S. J. L. Total Scattering Experiments. In *Underneath the Bragg Peaks: Structural Analysis of Complex Materials*; Takeshi, E., Billinge, S. J. L., Eds.; Pergamon, 2012; pp 113–158. <https://doi.org/10.1016/B978-0-08-097133-9.00004-6>. (92)
- Christiansen, T. L.; Cooper, S. R.; Jensen, K. M. Ø. There's No Place like Real-Space: Elucidating Size-Dependent Atomic Structure of Nanomaterials Using Pair Distribution Function Analysis. *Nanoscale Adv.* **2020**, *2* (6), 2234–2254. <https://doi.org/10.1039/D0NA00120A>. (93)
- Terban, M. W.; Billinge, S. J. L. Structural Analysis of Molecular Materials Using the Pair Distribution Function. *Chem. Rev.* **2022**, *122* (1), 1208–1272. <https://doi.org/10.1021/acs.chemrev.1c00237>. (94)
- Bennett, T. D.; Cheetham, A. K. Amorphous Metal–Organic Frameworks. *Acc. Chem. Res.* **2014**, *47* (5), 1555–1562. <https://doi.org/10.1021/ar5000314>. (95)
- Singh, H. P. Determination of Thermal Expansion of Germanium, Rhodium and Iridium by X-Rays. *Acta Crystallogr. Sect. A* **1968**, *24* (4), 469–471. <https://doi.org/10.1107/S056773946800094X>. (96)
- Shimizu, K.; Oda, T.; Sakamoto, Y.; Kamiya, Y.; Yoshida, H.; Satsuma, A. Quantitative Determination of Average Rhodium Oxidation State by a Simple XANES Analysis. *Appl. Catal. B Environ.* **2012**, *111–112*, 509–514. <https://doi.org/10.1016/j.apcatb.2011.11.002>. (97)
- Kalecińska, E.; Jezierski, A.; Kaleciński, J.; Pruchnik, F.; Jeżowska-Trzebiatowska, B. The Radiation Chemistry of Rhodium Complexes in Aqueous Alcoholic Systems. *Int. J. Radiat. Appl. Instrumentation. Part C. Radiat. Phys. Chem.* **1990**, *36* (2), 109–112. [https://doi.org/10.1016/1359-0197\(90\)90223-5](https://doi.org/10.1016/1359-0197(90)90223-5). (98)
- Kalecińska, E.; Kaleciński, J.; Pruchnik, F. P. Radiation Reduction of Binuclear Rh(II) Complexes in Aqueous-Methanol Solutions. *J. Radioanal. Nucl. Chem.* **1998**, *232* (1–2), 97–101. <https://doi.org/10.1007/BF02383721>. (99)
- Pruchnik, F.; Jezierski, A.; Kalecińska, E. Electron Paramagnetic Resonance Study on Radiation Reduction of Dirhodium(II) [Rh₂(O₂CR)₄] and [Rh₂Cl₂(O₂CR)₂(N₃)₂] Complexes. *Polyhedron* **1991**, *10* (22), 2551–2557. [https://doi.org/10.1016/S0277-5387\(00\)81329-7](https://doi.org/10.1016/S0277-5387(00)81329-7). (100)
- Eastland, G. W.; Symons, M. C. R. Electron Addition to Dirhodium Complexes: An Electron Spin Resonance Study. *J. Chem. Soc. Dalton Trans.* **1984**, No. 10, 2193. <https://doi.org/10.1039/dt9840002193>. (101)
- Nakamura, E.; Yoshikai, N.; Yamanaka, M. Mechanism of C–H Bond Activation/C–C Bond Formation Reaction between Diazo Compound and Alkane Catalyzed by Dirhodium Tetracarboxylate. *J. Am. Chem. Soc.* **2002**, *124* (24), 7181–7192. <https://doi.org/10.1021/ja017823o>. (102)
- Powers, I. G.; Uyeda, C. Metal–Metal Bonds in Catalysis. *ACS Catal.* **2017**, *7* (2), 936–958. <https://doi.org/10.1021/acscatal.6b02692>. (103)
- Legrand, A.; Craig, G. A.; Bonneau, M.; Minami, S.; Urayama, K.; Furukawa, S. Understanding the Multiscale Self-Assembly of Metal–Organic Polyhedra towards Functionally Graded Porous Gels. *Chem. Sci.* **2019**, *10* (47), 10833–10842. (104)

Rhodium-based metal–organic polyhedra assemblies for selective CO₂ photoreduction

- <https://doi.org/10.1039/C9SC04543K>.
- (90) Pruchnik, F. P. Structure and Reactivity of Rhodium(II) Complexes. *Pure Appl. Chem.* **1989**, *61* (5), 795–804. <https://doi.org/10.1351/pac198961050795>.
- (91) Yan, Z.; Du, M.-H.; Liu, J.; Jin, S.; Wang, C.; Zhuang, G.-L.; Kong, X.-J.; Long, L.-S.; Zheng, L.-S. Photo-Generated Dinuclear {Eu(II)}₂ Active Sites for Selective CO₂ Reduction in a Photosensitizing Metal-Organic Framework. *Nat. Commun.* **2018**, *9* (1), 3353. <https://doi.org/10.1038/s41467-018-05659-7>.
- (92) Probst, B.; Rodenberg, A.; Guttentag, M.; Hamm, P.; Alberto, R. A Highly Stable Rhenium–Cobalt System for Photocatalytic H₂ Production: Unraveling the Performance-Limiting Steps. *Inorg. Chem.* **2010**, *49* (14), 6453–6460. <https://doi.org/10.1021/ic100036v>.
- (93) Reithmeier, R.; Bruckmeier, C.; Rieger, B. Conversion of CO₂ via Visible Light Promoted Homogeneous Redox Catalysis. *Catalysts* **2012**, *2* (4), 544–571. <https://doi.org/10.3390/catal2040544>.

Rhodium-based metal-organic polyhedra assemblies for selective CO₂ photoreduction

